Effects of Edge Shapes on Thermal-Fluid Processes in Oscillatory Flows

Olusegun M. Ilori[1,*], Artur J. Jaworski[2], Xiaoan Mao[3], Olawale S. Ismail[4]

[1] School of Engineering, University of Bolton, Bolton, BL3 5AB, United Kingdom
[2] School of Computing and Engineering, University of Huddersfield, Queensgate, Huddersfield HD1 3DH, United Kingdom
[3] Faculty of Engineering, University of Leeds, Leeds, LS2 9JT, United Kingdom
[4] Faculty of Technology, University of Ibadan, Ibadan, Nigeria

*corresponding author. Tel.: +44 (0) 120 490 3031
E-mail address: o.ilori@bolton.ac.uk (O.M. Ilori)

Keywords:

Oscillatory Flows,
Edge-Shape,
Drive Ratio,
Heat Transfer,
Thermal Potential

ABSTRACT

Thermoacoustic machines, Stirling engines or coolers, and pulse tube coolers are examples of energy systems that operate based on oscillatory flow principles. This class of technology would achieve an improved efficiency from appropriately designed heat exchangers, stacks, regenerators and thermal buffer tubes. In this paper, heat transfer and oscillatory flow behaviour in three identical parallel-plate heat exchangers, one 'heat source' positioned between two 'heat sinks', are investigated using numerical method. The effect of different plate edge shapes on heat transfer, flow structures and acoustic pressure drop are examined at a selected drive ratio of 0.3 – 2.0%. Flow parameters show a strong dependency on drive ratio and flow direction, especially at low excitation where gas displacements are below or comparable to the heat exchanger length. Cone edge shape minimises the flow complexity better than other shapes with a negligible effect on the heat transfer. The result of this study will benefit the design and development of compact and high-efficiency heat exchangers for the next generation of oscillatory-flow energy and thermal management systems.

1.0 INTRODUCTION

A variety of energy and thermal management systems such as thermoacoustic devices, pulse tube coolers, and Stirling engines or coolers in cryogenic applications can achieve high efficiency because they rely on an acoustically induced working fluid to do energy transfer within their heat exchange components – heat exchangers, stacks, regenerators, and thermal buffer tubes. However, it is crucial to first understand thermalfluid processes in oscillatory flows, especially between the solid boundary and oscillating gas, from a component design perspective. Here, the challenge is to design compact and thermally efficient internal components because of the relatively short acoustic displacement amplitudes of the oscillating gas. Simultaneously, the flow losses due to geometrical discontinuity and changes in flow directions must be minimised to prevent loss of system efficiency (Wheatley et al., 1983; Olson and Swift, 1997).

For a few decades now, heat transfer and flow structures in oscillatory flows have been studied theoretically, numerically, experimentally or through a combination of these methods by researchers around the world (Kurzweg, 1986; Mackley and Stonestreet, 1995; Wang and Vanka, 1995; Swift, 2001; Oddy et al., 2001; Sert and Beskok, 2002: 2003; Paek et al. 2005). Piccolo and Pistone (2006) integrated linear acoustic theory through a numerical calculus with a simplified energy conservation model to estimate the optimal heat exchanger (HEX) length and magnitude of the heat transfer between gas and solid walls of the thermoacoustic system. Besnoin and Knio (2004) numerically investigated flow interaction within a stack and HEXs using a vorticity-based scheme for stratified flow. Mozurkewich (1998) developed an analytical model based on parallel-plate geometries for stack and HEX. Assumptions of laminar flow and gas temperature variation along the HEX length or stack were imposed. They observed that the gas temperature within the HEX could be quite non-uniform. The unsteady characteristic of heat transfer processes in a parallel plate structure was studied by Shi et al. (2010) through PLIF measurement techniques. The authors obtained a 2D temperature distribution of the gas around a parallelplate HEX as a phase function in an acoustic cycle and obtained a space-cycle Nusselt number (*Nu*) against the Reynolds number. The thermal potential in their heat transfer coefficient expression is obtained by subtracting the wall temperature from the channel's midpoint temperature. Jaworski et al. (2009) and Yu et al. (2014) used a combination of experimental and numerical methods to evaluate flow conditions and heat transfer in parallel plate structures. In the studies above, parallel plate geometries with square-edge shape (i.e., 90° edges) were used for investigations, and the effect of the channel edgeshape on flow and heat transfer was omitted. A few studies on numerical modelling of minor losses in oscillatory flow exist, e.g., Morris et al. (2004). Mohd-Saat (2013) used a CFD approach to study thermal-fluid processes inside a set of square-edge parallel-plate structures and at a drive ratio (DR) of 0.3 to 0.83% to replicate the experimental condition of Shi et al., 2010. The author reported a good match between their results and the test data and observed laminar oscillatory flows in the parallel plates (simulation and experiment) at a low DR $\leqslant$ 0.3%. Also, they found that numerical turbulent and laminar models gave identical results at this operating condition. Merlki and Thomann (1975) have shown experimentally that at a critical Reynolds number (Re_{crit}) of ~400, a transition from laminar flow to turbulence occurred in circular pipes.

Channel edge shapes of heat exchange components in oscillatory flow are important in designing and developing high-efficiency systems. It has been found by Cao et al. (1996) that the time-averaged heat transfer rate across the stack plate was concentrated at the edges. This result was later by Mozurkewich (1998) using an analytical boundary value method, observing that the time-averaged heat transfer is concentrated over the area that is of the order of the gas displacement amplitude. In the numerical study of Zoontjens et al. (2009), it was further shown that the stack plate half-thickness has a profound influence on the flow structure and heat flux distribution at the edges of the plate. The authors suggest that the generation of vortices around the stack region can be altered by plate thickness. In a different CFD study by the same authors, they showed that using a stack with a round edge could improve the cooling rate and the overall coefficient of performance of thermoacoustic refrigerator (Zoontjens et al., 2008). The authors investigated the effect of different edge shapes (except a cone edge shape) on system performance and observed that a round edge shape decreases the flow resistance and acoustic streaming at high amplitudes. However, the authors ignored the effects of resonator diameter and duct surfaces and used a half plate stack of infinite width and plate count located in a theoretical half-wavelength resonator operating at sub-atmospheric pressure. Their numerical model used a laminar viscous model to simulate high amplitude excitation known to be in the turbulent region (Merlki and Thomann, 1975; Olson and Swift, 1997) and require turbulence models (Ilori et al., 2014; Mohd-Saat, 2017). Therefore, an opportunity to considered other edges shapes and high accuracy simulation techniques does exist. Also, the effect of proximity of other components near the stack extremities needs to be understood.

To improve oscillatory flow conditions and minimise nonlinear effects associated with geometrical discontinuity, Smith and Swift (2003) used a rounded edge shape at the inlet and outlet of flow channels in their experiments. Marx et al. (2008) studied the unsteady effects at geometrical discontinuities in acoustic ducts. They considered the impact of the transition's curvature radius and the displacement amplitude in the pressure and energy losses calculation. Zhao and Cheng (1995) experimentally investigated the oscillatory convective heat transfer in a pipe with a rounded entrance and exit channel edge that was subjected to reciprocating flow. Their pipe was heated uniformly, and the thermal potential was obtained by subtracting the wall temperature from the fluid temperature at the inlet or outlet of the pipe. Aben et al. (2009) carried out 2D PIV experiments to study the vortex formation at the end of a parallel-plate stack using different edge shapes at an adiabatic condition. Weiyang and Fatimah (2016) considered edge shapes of parallel structures consisting of hot and cold plates placed in direct contact with each other. The authors considered a single drive ratio of 0.3%. However, a range of high excitations are used in a real system, and heat exchange components are separated with gaps that result from the geometric discontinuity due to different pattern and porosity of flow channels from individual elements. Takeyama (2018) experimentally studied the flat and spherical edge shapes of components of a coaxial thermoacoustic system to determine the influence of the inner tube length and the edge shapes of the outer tube on the energy conversion. It was concluded that the edge shape is an important design consideration for achieving high efficiency in a coaxial system. A recent study by Tartibu and Kunene (2019) considered similar edge shapes to Takeyama (2018) for a stack located in high amplitude excitation using the CFD approach. The authors focused on acoustic streaming but did not discuss heat transfer or compare their results with theoretical or experimental data.

It should be noted that the research works mentioned above used either a single or a pair of simplified geometries for their investigations. Also, studies that used real HEXs (e.g., Brady, 2011; Kamsanam et al., 2016) have reported that the conductive heat loss through the working fluid is difficult to estimate because of unsymmetrical arrangement, which suggests that a more accurate heat balance calculation can be obtained using symmetrically arranged HEXs. Also, the nonlinear flow behaviour associated with the geometrical discontinuity can be minimised using an appropriately designed channel edge shape. Interestingly, modern manufacturing techniques such as additive manufacturing can produce inherently complex shapes (Wong and Hernandez, 2012) and allow the design and manufacture of heat exchange components with edge shapes. Currently, oscillatory flow data are relatively scarce compared to the extensive data available for steady flow (Kays and London, 1964). Therefore, numerical investigations are necessary to complement the available experimental data to enhance the understanding of heat transfer processes in oscillatory flows.

This paper focuses on the effect of edge shapes on heat transfer, flow behaviour and oscillatory pressure drop of HEXs, using a CFD approach. The velocity profile, pressure and temperature fields, heat fluxes in the form of Nusselt number (*Nu*), flow behaviour and the pressure drop due to minor losses are examined against the system *DR*, defined as the ratio of the maximum pressure amplitude to the mean pressure in the system. The HEX is parallel plates with leading and trailing edges (depending on flow direction) of different shapes – square, cone, ogive, and round. The significance of this study is that changes in the heat transfer characteristic can be linked to a specific flow behaviour such as vortex shedding and turbulence. It is also envisaged that the symmetric arrangement of HEXs will facilitate an improved heat transfer performance estimation, leading to a reliable design guideline for heat exchange components under oscillatory flow conditions. Furthermore, the system performance can be improved by using heat exchange components with cone edge shapes to minimise losses associated with the geometrical discontinuity between components and changes in directions in oscillatory-flow devices.

2.0 Computational Model

This CFD study is developed based on the experimental setup described in (Ilori et al., 2018). The test data from the setup is used as the initial and boundary conditions in the simulation. Furthermore, the simulation results are compared to the analytical solution and the available test data. The overview of the setup schematic is shown in Fig. 1. It is 9.8 m long and consists of a test section, a cylindrical resonator, and an acoustic driver (Fig. 1a). The test section is positioned at 4.29 m from the pressure antinode at the closed end of the resonator, p_o ($x = 0$). Three identical crossflow HEXs are arranged symmetrically in the test section for characterisation under oscillatory flow conditions. The acoustic driver excites the pressurised helium gas (chosen because of its low Prandtl number). Further detail about the test rig is not repeated here since it has been published elsewhere.

2.1 Numerical Domain

Fig. 1b is a 2D replica of the test section in the experimental setup. It is chosen as the computational domain and has a length (L) of 900 mm. The axial location (x) in the direction of the acoustic propagation is normalised by L (i.e., x/L). The inlet and outlet positions are at distances x/L = 4.27 and x/L = 5.27 from the pressure antinode (p_o), respectively. Three identical parallel plates are arranged in series with a 4 mm horizontal gap between two adjacent HEX set, irrespective of the edge shape. A hot heat exchanger (HHX) is placed between two cold heat exchangers (CHX1 and CHX2). Fig. 1c shows all the edge shapes. The square edge has 90° sharp corners, The cone edge has a divergence angle (α) of 34.8°, the ogive edge has an ogive-like shape with a curvature radius of 7 mm, and the round-edge is a half-circle with a radius of 1.25 mm. For every simulation case, three HEXs (Fig. 1b) with the same edge shape are used as a set. There are nine flow channels in each HEX with a flow length (l) of 28 mm, including the edge shape. The porosity [$\sigma = d/(h + d)$] is 54.5%, and the domain length (L) is chosen such that the flow is not disturbed near the domain inlet and outlet boundaries to ensure that flow structures in the vicinity of HEXs is not influenced by any unsteadiness from the upstream or downstream regions.

Thermal and viscous penetration depths are defined as $\delta_k = \sqrt{2k_f/\omega\rho_m c_p} = 0.99$– 1.05 mm and $\delta_v = \sqrt{2\mu/\omega\rho_m} = 0.82$– 0.86 mm for the investigated range of temperature (15 – 50°C), where k_f, ω, ρ_m, c_p, and μ are thermal conductivity, angular frequency, mean density, isobaric heat capacity and dynamic viscosity. The Prandtl number, $Pr = (\delta_v/\delta_k)^2 = \mu c_p/k_f$ =1.46 – 1.49. The drive ratio (DR) is the pressure amplitude at the antinode divided by the mean pressure in the system, i.e., $DR = |p_0|/p_m \times 100\%$. The wavelength is defined as $\lambda = c/f$, where c and f are the speed of sound and frequency, respectively. The acoustic Reynolds number is described as $Re = \rho u_{1,mid}\, d/\mu$, where $u_{1,mid}$ is the velocity amplitude at the centre of HHX (x/L = 4.77) (Wakeland and Keolian, 2004; Tang et al., 2014). Locations *x/L* = 4.72, 4.75 4.79 and 4.82 (i.e. points 1, 2, 3, and 4 in Fig. 1b) correspond to positions of thermocouples and pressure transducers in the test section. Locations a, b and c are in the central flow channel of CHX2, at *x/L* = 4.79, 4.80 and 4.81, respectively. Fig. 2 shows the definition of flow directions, consisting of twenty phases in one acoustic cycle. Phases $\phi 1$ – $\phi 10$ denote the suction stage while phases $\phi 11$ – $\phi 20$ represent the ejection stage.

2.2 Governing Equations

Time-dependent Navier-stokes (N-S) equations are solved in ANSYS Fluent 17.0 using finite volume method (FVM) (ANSYS Inc., 2016; Versteeg and Malalasekera, 2007). Reynolds Averaged N-S (RANS) equations are used (Nijeholt et al.,2005; MohdSaat, F.A.Z., 2013; Ilori et al. 2014), which are derived from N-S equations by time-averaging the transport and energy equations, with variables (such as velocity) decomposed into mean and fluctuating components, $\phi = \bar{\phi} + \phi'$. In a conservative form, the continuity, momentum, energy equations are written as:

$$\frac{\partial \rho}{\partial t} + \frac{\partial}{\partial x_j}(\rho u_i) = 0 \tag{1}$$

$$\frac{\partial(\rho u_i)}{\partial t} + \frac{\partial(\rho u_i u_j)}{\partial x_j} = -\frac{\partial p}{\partial x_i} + F_i + \frac{\partial}{\partial x_j}(\tau_{ij})_{eff} + \frac{\partial}{\partial x_j}\left(-\overline{\rho u'_i u'_j}\right) + + \frac{\partial}{\partial x_i}\left(-\overline{\rho {u'_i}^2}\right) + S_G \tag{2}$$

$$\frac{\partial}{\partial t}(\rho E) + \frac{\partial}{\partial x_i}[u_i(\rho E + p)] = \frac{\partial}{\partial x_j}\left(k_{eff}\frac{\partial T}{\partial x_j} + u_i(\tau_{ij})_{eff}\right) + S_N \tag{3}$$

where *F*, S_G and S_N are the external force, and user-defined source terms in ANSYS Fluent, E and κ are the internal energy and turbulent kinetic energy. The effective stress tensor is defined as:

$$\left(\tau_{ij}\right)_{eff} = \mu\left(\frac{\partial u_j}{\partial x_i} + \frac{\partial u_i}{\partial x_j}\right) - \frac{2}{3}\mu_{eff}\frac{\partial u_k}{\partial x_k}\delta_{ij} \tag{4}$$

Eq. 4 represents the stress tensor under the influence of turbulence with effective viscosity, $\mu_{eff} = \mu + \mu_t$, where μ is the laminar viscosity and μ_t turbulent viscosity. Similarly, the effective thermal conductivity $k_{eff} = k_f + k_t$ is the sum of mean thermal conductivity, k_f and turbulent conductivity k_t calculated as $k_t = \mu_t c_p / Pr_t$. The turbulence Prandtl number (Pr_t) has a constant of 0.85. The turbulent viscosity (μ_t) is calculated using the turbulence model. The Reynolds Stresses term, $-\overline{\rho u'_i u'}_j$ are solved through additional equations provided by the turbulence model.

$$-\overline{\rho u'_i u'}_j = \mu_t\left(\frac{\partial u_j}{\partial x_i} + \frac{\partial u_i}{\partial x_j}\right) - \frac{2}{3}\left(\rho\kappa + \mu_t\frac{\partial u_k}{\partial x_k}\right)\delta_{ij} \tag{5}$$

The Kronecker delta δ_{ij} is included to correctly model the normal component of Reynolds Stress. In addition to the governing equations, pressure and density are related through the ideal gas equation:

$$p = \rho RT \tag{6}$$

Shear Stress Transport (SST) k-ω turbulence model (Menter, 1994), Pressure Implicit Splitting Operators (PISO) algorithm, and second-order discretisation are used in all simulation cases. Default values are retained for constants in the SST k-ω turbulence model. Calculations start at an assigned time step size, $\Delta t = 1/N_f$, where N_f is the number of time steps over a complete flow cycle. Here, N_f = 600 as determined after the sensitivity check on the time discretisation. Residuals are allowed to fall below 10^{-5} for the continuity, momentum, and turbulence, and 10^{-7} for energy equations.

2.3 Initial and Boundary Conditions

Temperature-dependent viscosity and thermal conductivity are defined as (Bird et al., 2006, Incropera et al., 2007):

$$\mu = 1.99 \cdot 10^{-5} \cdot (T/T_{ref})^{0.68} \qquad k_f = 0.152 \cdot (T/T_{ref})^{0.72} \tag{7}$$

where subscript ‘ref’ denotes the reference temperature (here, T_{ref} = 300K).

pressure amplitudes and phases measured at the inlet and outlet locations (cf. Fig. 1) in experiments are used as acoustic boundary conditions in the simulation and described by:

$$p_{1,in}(x,t) = p_{1,in} \cdot cos(\, \omega t + \phi_{in}) \tag{8}$$

$$p_{1,out}\,(x,t) = p_{1,out} \cdot cos(\omega t + \phi_{out}) \tag{9}$$

Turbulence boundary conditions are specified in terms of turbulence intensity and length scale as (Russo and Basse, 2016; ANSYS Fluent, 2016):

$$I = 0.16(Re_{1(in,out)})^{-0.125} \qquad \ell = 0.07D \tag{10}$$

The acoustic Reynolds number is defined as $Re_{1(in,out)} = \rho_{ref} u_{1(in,out)} D/\mu_{ref}$ for the domain inlet and outlet. The acoustic velocities in the $Re_{1(in,out)}$ is calculated as:

$$u_{1,in}(x) = \frac{p_o}{\rho_m c} sin(\, k' x_{in}) \tag{11}$$

$$u_{1,out}\,(x) = \frac{p_o}{\rho_m c} sin(\, k' x_{out}) \tag{12}$$

The density and dynamic viscosity at 300 K (the reference temperature) are used in the acoustic Reynolds number. CHX1 and CHX2 are maintained at a constant temperature of 15ºC, and HHX is held at 50ºC to replicate the experimental thermal boundary conditions. Additional thermal conditions are specified at the inlet and outlet as:

$$\frac{\partial T}{\partial x}|x_{in}, x_{out} = 0 \tag{13}$$

Condition (13) is used to keep temperatures of cells next to boundaries equal to that of the reversing flow. The resonator wall is modelled as adiabatic, and Non-slip boundary conditions are applied to all walls (CHX1, HHX, CHX2 and resonator).

The following dimensionless variables are introduced:

$$\delta = \frac{y}{d} \tag{14}$$

$$U = \frac{u_1}{u_{1,max}} \tag{15}$$

$$\theta = \frac{T_f - T_w}{T_h - T_c} \tag{16}$$

Expressions (14) is the vertical distance in the flow channel normalised by the plate separation distance. The velocity amplitude in equation (15) is normalised using $u_{1,max}$ which is the peak velocity amplitude in the positive oscillatory flow direction (cf. Fig. 2). In equation (16), the temperature is normalised with the fluid, wall, reference hot (here 50°C) and reference cold (here 15°C) heat exchanger temperatures (Yu et al., 2014; Zhao and Cheng, 1995).

2.4 Mesh Sensitivity

A mesh convergence check was performed to ascertain the simulation results' independence on mesh refinement (Roache, 1994). The mesh resolution was refined until the solution became unaffected for the Ogive-edge HEX. Here, converged solutions from mesh counts of 43,348 (C1), 70,376 (C2), 113,979 (C3) and 179,140 (C4) are compared for the mesh sensitivity check. Mesh count C3 was found sufficient for obtaining solutions independent of the mesh size. The maximum y+ everywhere in the wall region is 0.327 (i.e.

y+ < 1). Fig. 3a shows the centerline velocity amplitude (*x/L* = 4.80) in the CHX2 with a square edge shape. Once the C3 mesh is selected for the study, similar mesh size is used on all other edge shapes. It was ensured that fine mesh is present everywhere in the simulation domain, and twelve grid points are present within the boundary layer and the vicinity of HEXs to properly resolve heat transfer and flow conditions in the boundary

layer.

2.5 Numerical Model Validation

An analytical expression for laminar flow in a channel formed by parallel plates with squared edge-shape was proposed by Swift (2001) and is defined as:

$$u(y,t) = Re\left(\frac{u_{c2}}{\sigma}\left\{1-\frac{cosh\,[(1+i)(y-y_o)/\delta_v]}{cosh\,[(1+i)y_o/\delta_v]}\right\}e^{i\omega t}\right) \quad (17)$$

where $y = 0$ at the central channel of HHX and $y_o = d/2$. The author found that the porosity of the geometry must be considered if the plate thickness and comparable to the separation distance between two plates. The solution from expression (17) is compared with the square-edge simulation results at *DR* = 0.3%, where the flow is considered laminar (Merlki and Thomann, 1975; Shi et al., 2010; Ilori et al., 2014). Fig. 3b shows the comparison between the centreline velocity amplitude in the CHX2 and the analytical solution with the porosity of the HEX duly considered. The maximum discrepancy between the two results is below 3%.

Furthermore, the simulation results are compared to the test data (Ilori et al.,2018) in the form of pressure amplitudes and the gas temperature near the edges of HHXs to gain increased confidence in the numerical solution. Fig. 3c shows the predicted and measured pressure amplitudes at location *x/L* = 4.79 (cf. Fig. 1b). Both results are in good agreement, with a maximum discrepancy below 6% for the suction and ejection stages. In Fig. 3d, the measured gas temperature was compared to predictions at T1, T2, T3 and T4 near CHX1, CHX2, and HHX edges. Similar trends can be observed in both results for all the locations. At *DR* = 0.7%, the gas displacement amplitude ($\xi_1 = u_1/\omega$) is 27.98mm. The maximum difference between measured and predicted gas temperatures for the three HHXs is below 1% for 0.3 ≤ *DR* ≤ 1.5%. This result is consistent with the findings in Piccolo and Pistone (2006) at a similar range of operating conditions. The authors also used parallel plate structures with square edge shape in their numerical investigation.

3.0 RESULTS AND DISCUSSION

Initial simulation studies focused on mesh sensitivity and model validation, as discussed in section 2.5. With sufficient confidence in the numerical method, further investigation of HEXs performance with other edge shapes was carried out and discussed in terms of velocity and temperature fields, heat transfer processes and acoustic pressure drop (Δp_1). Effects of laminar and turbulence models and adiabatic and imposed constant temperature on walls on thermal-fluid processes in oscillatory flows have been reported elsewhere (Ilori et al., 2018); hence, such details are not repeated here.

3.1 Effect of Edge Shape on Velocity Profile

Table 2 summarises simulation results for all edge shapes (square, cone, ogive, and round). The corresponding range of values of ξ_1 are 12–76.6 mm, 10.9–73.7 mm, 11.4–75.2 mm and 11.8–76.5 mm for square, cone, ogive, and round edge shapes, respectively, at acoustic Reynolds number (Re_1) of 96 – 672, for all *DRs*. The CHX2 is the closest to the velocity antinode in the test rig, and locations around it are chosen for data sampling to determine the influence of edge shape. Fig. 4 shows the velocity at CHX2 inlet (*x/L* = 4.79) (cf. Fig. 1c). The velocity profiles are plotted for y/2, and comparisons for velocity phases, $\phi 1$, $\phi 4$, and $\phi 7$ are made for edge shapes at $0.3 \leq DR \leq 2.0\%$. The effect of cone edge shape appears to be more noticeable compared to other edge shapes. The influence is within the viscous penetration depth, δ_v =0.84 mm (average value), at *DR* = 0.3% and 0.65%. Fig. 5 shows velocity profiles at *x/L* = 4.80 and $\phi 4$ for *DR* = 0.65% and 1.0%, which indicate a diminished effect of edge shapes on the fluid flow. In Fig. 6, the cone-edge has velocity amplitudes of 10%, 12% and 4% lower at *DR*s of 0.3%, 0.65% and 2.0%, respectively, in comparison to the square-edge. Similarly, the ogive-edge is 6%, 7% and 1.8% lower, while the round-edge is 2%, 1.4% and 0.2% lower, for the *DR*s.

Fig. 7 shows the comparison between flow behaviour at *DR*s 0.3 and 1.0% ($\phi 7$) in the form of vorticity contours, calculated as $\omega_v = \partial v/\partial x - \partial u/\partial y$, where u and v are velocity components in *x* and *y*-directions. In Fig. 7a, a pair of vortex structures can be seen in the flow channels and at the end of the CHX2 (right side) where they remain attached. The pair of vortices are symmetrical about the centreline of the channel and have equal but opposite strengths. All edge shapes appear to have a similar effect due to low acoustic displacement at *DR* = 0.3%. However, at a much higher displacement at *DR* = 1.0% (Fig. 7b), a different flow behaviour can be observed at the edges. The pair of vortices has become elongated and distorted for the square-edge, while they are elongated, nearly symmetrical about the centreline, and less distorted for other edge-shapes. The difference in flow behaviour means a difference in HX's heat transfer and pressure drop performance due to each edge shape. The vortex strength at the end of plates (in the wake) for 1.0% *DR* can create a strong disturbance if pushed back into the flow channel. Corners of square edge shape caused more disruptive flow separations and generated more vortices, which can cause increased energy dissipation and pressure losses. This could explain the observed distortion in the acoustic pressure drop profile (Fig. 12) that will be discussed in the later section.

3.2 Effect of Edge Shape on fluid temperature

Table 2 shows gas temperature values at the CHX2 inlet. The gas temperatures increase in the order of $T_{sq} > T_{rn} > T_{og} > T_{cn}$, at *DR* = 0.3%, while the order changed to $T_{cn} > T_{og} > T_{rn} > T_{sq}$, at *DR* = 0.65%. Fluid temperatures are higher *DR* = 0.65% than all other *DR*s for all edge shapes, which indicates that it could be favourable for heat transfer consideration. Fig. 8 shows the temperature profiles at CHX2 inlet (x/L = 4.79) for 0.3 ≤ *DR* ≤ 2.0%. An annular effect [14, 17] can be observed at ϕ7 for all edge shapes at *DR* = 1.0%. At *DR* of 1.5 – 2.0%, a similar effect is present at ϕ10 and ϕ7. Fig. 9 shows that the time-averaged temperature strongly depends on the *DR* at the flow channel inlet, centreline midpoint and outlet locations location a, b and c in Fig. 1c, with temperature gains from both CHX1 and CHX2 having similar trends to temperature changes in HHX at *DR* > 1.0%. The rate of decrease within the HHX channel is very rapid at 0.3 ≤ *DR* ≤ 0.7%. Likewise, the rate of increase in temperature in the CHX1 and CHX2 is rapid at the same range of *DR*, indicating that displacement amplitude is below or comparable to the heat exchanger length. At *DR* > 0.7%, a slight decrease (HHX) or increase (CHX1 and CHX2) can be seen, which indicates a lower heat transfer rate that can be attributed to the displacement amplitude been larger than the heat exchanger length.

At the inlet of CHX2, the fluid temperature is warmer than the channel midpoint at $DR \leq 0.65\%$ due to the influence of the warmer fluid exiting the HHX. The gas displacement amplitude was not large enough to rapidly move the fluid to the heat exchange area of the CHX2, where it can reject heat at heat sink (CHX2) temperature, hence, causing an imbalance between heat gained and heat rejected. A similar effect can be observed at the outlet of CHX1 (Fig. 9c). The cone edge shape yielded the highest temperature within the HHX, followed by ogive, round, and square edge shapes for all cases. Within the CHX1 and CHX2, the order of influence was the opposite. From

temperature profiles in Figs 8 and 9, it is thus clear that the edge shapes influenced the heat transfer in heat exchanger channels. The link between the velocity and temperature amplitudes can also be seen in Figs 4 to 9. However, as previously observed in (Mozurkewich, 1998), the gas temperature of the exchanger can be quite non-uniform rather than anchored to the wall temperature when observed at an individual phase within the acoustic cycle. Therefore, the effect of edge shape on the global heat transfer rate will be examined next.

3.3 Effect of Edge Shape on Heat Transfer

The effect of edge shapes on HEXs' heat transfer behaviour is considered in this section. From the temperature profiles (shown in Fig. 8), heat flux values on HEX walls can be estimated to gain an insight into the heat transfer within the flow channels.

3.3.1 Heat flux calculation

The local heat flux as a function of axial location and phase is defined as:

$$q(x,\phi) = -k_f \left.\frac{dT(x,y,\phi)}{dy}\right|_{Wall} \tag{18}$$

Following a standard convention, the negative sign indicates heat transfer from the solid wall to the fluid, while the opposite is heat transfer from gas to a solid wall. A combination of the space-averaged and cycle-averaged local heat fluxes would yield the space-cycle averaged heat flux for the HEXs, which is given by (Shi et al., 2010; Zhao and Cheng, 1995)

$$q_{h,c1,c2} = \frac{1}{2\pi l}\int_0^{2\pi}\int_0^{l} q\,(x,\phi)\Big|_{Wall} dx d\varphi \approx \frac{1}{2\pi l}\sum_{i=0}^{2\pi}\left(\sum_{j=0}^{l} -k_h \left.\frac{\Delta T}{\Delta y}\right|_{Wall} .\,\Delta x_j\right).\,\Delta\,\phi_i \tag{19}$$

The local heat flux, $q(x,\phi)$, as a function of space and phase are obtained (ANSYS Fluent, 2016) and averaged over one flow cycle as indicated in equation (19). The heat flux is shown in Fig. 10 for $0.3 \leq DR \leq 2.0\%$. For the CHX1, HHX and CHX2, heat fluxes increase with the increase in *DR,* which are more rapid between $0.3 \leq DR \leq 1.0\%$ than the remaining *DR*s. According to the symmetric heat exchanger arrangement, the heat balance in terms of heat flux can be written as:

$$q_h = q_{c1} + q_{c2} \tag{20}$$

Equation (20) indicates that the heat flux from HHX should be equal to the combined heat fluxes from CHX1 and CHX2. However, the net heat flux from CHX1 and CHX2 is slightly higher than HHX's at each *DR*. For instance, the combined heat flux for CHX1 and CHX2 is 8.2% higher, at $DR = 0.3\%$ for the square edge. The imbalance is not accounted for in the numerical model due to the adiabatic wall condition. In the actual experiments, this would mean a heat leak to the surrounding. Fig. 10 shows heat fluxes having similar trends for the edge shapes. Square edge gave the highest heat fluxes at both low and high *DR* compared to other edge shapes, and this can be attributed to the effect of flow disturbances associated with this edge shape (cf. Fig. 7), which promotes heat transfer. The cone-edge gives the lowest heat fluxes. The maximum and minimum heat fluxes for square and cone edge shapes occurred at DR = 2.0% in the HHX with values of 3728 W/m^2 (square-edge) and 3596 W/m^2 (cone-edge). As previously remarked, the consideration here is twofold: on the one hand, the minimisation of acoustic pressure drop is desirable from the viewpoint of the overall efficiency of oscillatory flow systems. On the contrary, the reduction in the heat transfer performance of the heat exchanger is undesirable as this will impinge on the system's overall thermal performance. The edge shapes caused a slight reduction in the heat flux, especially at DR = 0.3%, which is about 40% (cone-edge), 27% (Ogive edge) and 8% (round edge), compared to the square-edge shape. At DR = 2.0%, this about 4%, less than 1%, and less than 0.5% for the edges, respectively. However, the heat flux loss vanished as DR increases especially at DR = 3.0%, which then makes the study more interesting as the practical oscillatory flow will normally operate at a much higher DR (Swift, 2001)

3.3.2 Nusselt number calculation

The local instantaneous Nusselt number is defined as

$$Nu(x,\phi) = \frac{h_{loc}(x,\phi)d_h}{k_f} \tag{20}$$

h_c is the local instantaneous heat transfer coefficient defined as:

$$h_c(x,\phi) = \frac{q(x,\phi)}{\Delta T(x,\phi)} \tag{21}$$

The thermal potential for heat transfer coefficient $\Delta T(x,\phi)$ is defined as $\Delta T(x,\phi) = T_w(x) - T_i(\phi)$. $T_i(\phi)$ is the mean of gas temperatures at x/L = 4.72, 4.75, 4.79 and 4.82 that is:

$$T_i(\phi) = \frac{T_{inlet}(\phi)+T_{exit}(\phi)}{2} \tag{22}$$

The thermal potential for heat flux is defined differently from the ones proposed by Zhao and Cheng (1995), Shi et al. (2010) and Wheatley et al. (1983). It should be noted that the choice of $\Delta T(x,\phi)$ is application dependent, and the definition here is based on the symmetrical heat exchanger arrangement. The space-cycle averaged *Nu* is defined for CHX1, HHX and CHX2 as

$$Nu_{h,c1,c2} = \frac{1}{2\pi l}\int_0^{2\pi}\int_0^{l} Nu\,(x,\phi)dxd\phi \approx \frac{1}{2\pi l}\sum_{i=0}^{2\pi}\left(\sum_{j=0}^{l} Nu(x,\phi)|_{Wall}.\Delta x_j\right).\Delta\,\phi_i \quad (23)$$

where subscripts *h*, c1, and c2 denote the *Nu* for HHX, CHX1, and CHX2, respectively. The space-cycle *Nu* as a function of *DR* is shown in Fig. 11. Overall, the numerical spaceaveraged *Nu* increases with *DR* and has a good match with the experimental values. The Nu increase is rapid for all edge shapes at DR < 0.65%, which becomes gradual at *DR* > 0.7%. This behaviour agrees well with the description in the literature and the thermoacoustic design guidelines (Swift, 2001; Piccolo and Pistone, 2006). The difference between the magnitudes of predicted and measured *Nu* at the considered *DR* can be attributed to some factors. Firstly, the experimental results are obtained for the flat-edge tube-heat exchanger configuration of Ilori et al. (2018), which has a slightly different geometry than the parallel-plate type in the simulation. Secondly, there is a difference in the calculation methods for heat transfer coefficients. In the experiment (Ilori et al., 2018), the heat transfer coefficient and the *Nu* were calculated from equations (24) and (25) as:

$$h = \frac{q}{\Delta T} \quad (24)$$

$$Nu = \frac{hl}{k} \quad (25)$$

where the *Nu* is in terms of heat exchanger length *l*.

Therefore, the highlighted difference in the calculation method could contribute to the observed difference.

3.4 Effect of Edge Shape on Acoustic Pressure Drop

Fig. 12a-c show the Δp_1 across CHX1, HHX, and CHX2. Data is sampled at locations *x/L* = 4.72, *x/L* = 4.75, *x/L* = 4.79, and *x/L* = 4.82 (points 1, 2, 3, and 4 in Fig. 1c). The result is presented as a function of time, normalised by the period of oscillation, i.e., $T_p = 1/f$ (Smith and Swift, 2003). Cone edge shape minimised the Δp_1 better than the other edge shapes, and this key for performance improvement of oscillatory flow devices. At 0.3<*DR*<0.65%, the edge shape effect on Δp_1 is less pronounced, as observed in the vorticity contours at *DR* = 0.3%. In Fig 12(a), the maximum Δp_1 is present at 0< t/T_p<0.3 in the suction phase of the acoustic cycle for *DR* > 0.3%. As the *DR* increases, the distortion in the Δp_1 profile increases significantly due to minor losses created by the sudden crosssection decrease. However, cone-edge shape exhibits a lower Δp_1 than the other edge shapes. The edge shape's influence on the Δp_1 shows a strong dependence on the *DR* and flow direction. Also, the influence of the HEXs' symmetrical arrangement can easily be inferred (Fig. 12a-c). At 0.3 < t/T_p < 0.5, has the lowest Δp_1 and the flow enters an ejection phase (0.5 < t/T_p < 1) the Δp_1 is at its lowest for all edge shapes. Fig. 12b shows the Δp_1 across the HHX. In the suction stage (0 < t/T_p < 0.5), the distortion in the Δp_1 is less pronounced than that of CHX1 in a similar stage. The magnitude of Δp_1 remains almost the same between the ejection stage in CHX1 and the suction stage in HHX. Similar behaviour is observed when the flow exits HHX and enters CHX2, as shown in Fig.12c. However, during the ejection stage in CHX2 at 0.5 < t/T_p < 1, the sudden increase in the cross-section increases the Δp_1 as seen in CHX1 previously. The cone edge minimised the

Δp_1 across the HEXs compared to the other edge shapes. It is noteworthy that the Δp_1 may depend on the sampling location. However, the exact locations are used to compare the effects of the edge shapes; therefore, the plots reflect the role of each edge shape in minimising the Δp_1 across the three HEXs.

Fig. 13 shows the comparison between measured and predicted Δp_1 across HHX and CHX2 heat exchangers with square edge-shape. There is a qualitative agreement between the two results as the trends in both plots (Fig. 13a and b) are similar, and the effects of the sudden change in the cross-section and edge profile are present in both cases. However, the measured Δp_1 is considerably higher than predicted. This difference is as high as a factor of two at both suction and ejection stages ($0 < t/T_p < 0.5 < 1$). As previously remarked, the discrepancy in the results can be attributed to the geometry difference.

4. CONCLUSION

The effect of edge shapes on heat transfer and acoustic pressure drop in the oscillatory flow HEXs has been investigated numerically. The investigation was carried out for drive ratios of $0.3 \leq DR \leq 2.0\%$ for four different edge shapes – square, cone, ogive, and round. It was found that the heat transfer and the acoustic pressure drop show a strong dependency on the drive ratio for the studied edge shapes.

For the heat transfer, the square-edge and round-edge *Nu* values are higher than those of cone-edge and ogive edge. The wall heat fluxes and *Nu* increase with the increase in drive ratio for all edge shapes. The increase is rapid until DR = 0.7% and then became gradual. Furthermore, it was found that the thermal potential for the heat transfer coefficient can be defined to reflect the contribution of gas temperatures at the channel inlet and outlet to the HEXs performance.

Regarding the acoustic pressure drop (Δp_1), the cone edge shape gave the lowest value at all drive ratios, especially at drive ratios of $1.0 \leq DR \leq 2.0$ in the region of $0 < t/T_p < 0.3$ for the CHX1 and $0.5 < t/T_p < 0.8$ for CHX2. This is interesting since practical oscillatory-flow systems operate at much higher amplitudes. Therefore, this study suggests that the use of cone edge shape will be beneficial at high *DRs* and improve the performance of oscillatory flow systems. Future work will consider the determination of minor loss coefficients associated with a sudden change in the cross-section of the heat exchanger flow channels.

ACKNOWLEDGMENTS

Olusegun M. Ilori acknowledges the Petroleum Technology Development Fund (Ref. No. PTDF/E/OSS/PHD/IMO/395/11, 2012-2015) – a parastatal of the Ministry of Petroleum Resources in Nigeria. Artur J. Jaworski acknowledges funding from the Royal Society Industry Fellowship scheme (Ref. No. IF110094, 2012-2015) and EPSRC UK under HARP^2 Programme (Ref. No. EP/R023328/1, 2018-2021). Innovate UK is acknowledged for funding under the TITAN project (Ref. No. 131497).

REFERENCES

Aben, P.C.H., Bloemen, P.R., and Zeegers, J.C.H., 2009. 2-D PIV Measurement of Oscillatory Flow Around Parallel Plates. *Experiments in Fluids*, 46, pp. 631-431.

ANSYS Fluent 17.0.1, 2016, “User Manual,” ANSYS Inc.

Besnoin, E. and Knio, O.M., 2004. Numerical Study of Thermoacoustic Heat Exchangers. *Acta Acustica United With Acustica*, 90 (3), pp. 432-444.

Bird, R.B., Stewart, W.E., Lightfoot E.N. Transport Phenomena, John Wiley & Sons, Inc., 605 Third Avenue, New York, NY 10158-0012, 2nd Ed.

Brady J. F., 2011. The effects of Geometry and Adjacent Regenerators on Shell-And-Tube Heat Exchangers in Oscillatory Flows. PhD thesis, The Pennsylvania State University.

Cao, N., Olson, J. R., Swift, G. W., Chen, S, 1996. Energy Flux Density in a Thermoacoustic Couple. J. Acoust. Soc. Am., 99 (6), pp. 3456-3464.

Dieck, R. H., Steele, W. G., Osolsobe, G., 2005. Test Uncertainty. ASME PTC 19.1-2005. New York: The American Society of Mechanical Engineers.

Ilori, O.M., Jaworski, A.J., Mao, X., 2018. Experimental and Numerical Investigations of Thermal Characteristics of Heat Exchangers in Oscillatory Flow. *Applied Thermal Engineering*, 144, pp. 910-925.

Ilori, O.M., Mao, X., Jaworski, A.J., 2014. CFD-Simulation of Oscillatory Flow Around the Heat Exchangers of Thermoacoustic Devices. *Proceedings of the ASME 2014 International Mechanical Engineering Congress and Exposition. Volume 7: Fluids Engineering Systems and Technologies*. Montreal, Quebec, Canada. November 14–20, V007T09A052. ASME.

Incropera, F. P., DeWitt, D. P., Bergman, T. L., and Lavine, A. S., 2007. Fundamentals of Heat and Mass Transfer, 6th ed., John Wiley and Sons, New York

Jaworski, A. J., Mao, X., Mao X., Yu, Z., 2009. Entrance Effects in the Channels of the Parallel Plate Stack in Oscillatory Flow Conditions. *Experimental Thermal and Fluid Science*, 33(3), pp. 495-502.

Kamsanam, W., Mao, X., Jaworski, A.J., 2016. Thermal Performance of Finned-Tube Thermoacoustic Heat Exchangers in Oscillatory Flow Conditions. *International Journal of Thermal Sciences*, 101, pp. 169-180.

Kays, W. M., London, A. L., 1964. Compact Heat Exchangers. McGraw-Hill, New York.

Kim, J. H., Simon, T. W. and Viskanta, R., 1993. Journal-of-Heat-Transfer policy on reporting uncertainties in experimental measurements and results. *Journal of Heat Transfer-Transactions of the ASME*, 115(1), pp. 5-6.

Kurzweg, U.H., 1986. Temporal and Spatial Distribution of Heat Flux in Oscillating Flow Subjected to an Axial Temperature Gradient. *Int. J. Heat Mass Transfer*, 29 (12), pp. 1969–1977.

Mackley, M. R. and Stonestreet, P., 1995. Heat Transfer And Associated Energy Dissipation For Oscillatory Flow In Baffled Tubes. *Chemical Engineering Science*, 50 (14), pp. 2211-2224

Marx, D., Bailliet, H., and Valiere, J., 2008. Analysis of the Acoustic Flow at an Abrupt Change in Section of an Acoustic Waveguide Using Particle Image Velocimetry and Proper Orthogonal Decomposition. *Acta Acustica United with Acustica*, 94(4), pp. 54-65.

Menter, F. R., 1994. Two-Equation Eddy-Viscosity Turbulence Models For Engineering Applications. *AIAA Journal*, 32 (8), pp. 1598-1605.

Merlki P., Thomann, H., 1975. Transition to Turbulence in Oscillating Pipe Flow. *Journal of Fluid Mechanics*, 68 (3), pp. 567-575.

Moffat, R. J., 1988. Describing the Uncertainties in Experimental Results. *Experimental Thermal and Fluid Science*, 1(1), pp. 3-17.

Mohd Saat, FAZ, 2013. Numerical Investigations of Fluid Flow and Heat Transfer Processes in the Internal Structures of Thermoacoustic Devices. PhD Thesis, Dept. of Eng., Univ. of Leicester, UK.

Mohd Saat, FAZ., Jaworski, A.J., 2017. Numerical Predictions of Early Stage Turbulence in Oscillatory Flow across Parallel-Plate Heat Exchangers of a Thermoacoustic System. Appl. Sci. 7, pp. 673.

Morris, P. J., Boluriaan, S., Shieh, C. M., 2004. Numerical Simulation of Minor Losses Due to a Sudden Contraction and expansion in High Amplitude Acoustic Resonators. *Acta Acustica United with Acustica*, 90, pp. 393-409

Mozurkewich, G., 1998. A Model for Transverse Heat Transfer in Thermoacoustics. *J. Acoustic. Soc. Am*. 103(6), pp. 3318-3326.

Mozurkewich, G., 1998. Time-Average Temperature Distribution in a Thermoacoustic Stack. J. Acoust. Soc. Am., 103, pp. 380.

Nijeholt, J.A., Tijani, M.E.H., Spoelstra, S, 2005. Simulation of a Travelling-Wave Thermoacoustic Engine using Computational Fluid Dynamics. *J. Acoust. Soc. Am*. 118 (4), pp. 2265–2270

Oddy, M.H., Santiago, J.G., Mikkelsen, J.C., 2001. Electrokinetic Instability Micromixing. *Anal. Chem*. 73 (24), pp. 5822–5832.

Olson J.R., Swift, G.W., 1997. Acoustic Streaming in Pulse Tube Refrigerators-Tapered Pulse Tubes. *Cryogenics*, 37 (12), 769 – 776.

Paek, I., Braun, J.E., Mongeau, L., 2005. Characterising Heat Transfer Coefficients for Heat Exchangers in Standing Wave Thermoacoustic Coolers. *J. Acoust. Soc. Am*., 118 (4) pp. 2271–2280.

Piccolo, A., Pistone, G., 2006. Estimation of Heat Transfer Coefficients In Oscillating Flows: The Thermoacoustic Case. *International Journal of Heat and Mass Transfer*, 49 (910), pp. 1631-1642.

Roache, P. J., 1994. Perspective: A Method for Uniform Reporting of Grid Refinement Studies. Transactions-American Society of Mechanical Engineers, *Journal of Fluids Engineering*, 16, pp. 405-405.

Russo, F. and Basse, N.T. (2016). Scaling of Turbulence Intensity for Low-Speed Flow in Smooth Pipes. Flow Meas. Instrum., 52, pp. 101–114.

Sert, C., Beskok, A., 2002. Oscillatory Flow Forced Convection in Micro Heat Spreaders. *Numer. Heat Transfer A*. 42 (7), pp. 685–705.

Sert, C., Beskok, A., 2003. Numerical Simulation of Reciprocating Flow Forced Convection in Two-Dimensional Channels. *J. Heat Transfer*, 125, pp. 403–412.

Shi, L., Mao, X., Jaworski, A.J., 2010. Application of Planar Laser-Induced Fluorescence Measurement Techniques to Study The Heat Transfer Characteristics of Parallel-Plate Heat Exchangers in Thermoacoustic Devices. *Measurement Science and Technology*, 21**(**11), pp. 115-405.

Smith, B. L, and Swift, G. W., 2003. Power Dissipation and Time-Averaged Pressure in Oscillating Flow Through a Sudden Area Change. *J. Acoust. Soc. Am*. 113(5), pp. 24552463

Swift, G. W., 2001. Thermoacoustics: A Unifying Perspective for Some Engines and Refrigerators. Los Alamos National Laboratory, (Fifth Draft, LA-UR 99-895).

Takeyama, Y., 2018. Study on a coaxial thermoacoustic system: Effect of the Edge Shape on the Acoustic Intensity. *J. Acoust. Soc. Am.*, 144, pp. 1713.

Tang K., Yu J., Jin T., Wang Y.P., Tang W.T., Gan Z.H., 2014. Heat Transfer of Laminar Oscillating Flow in Finned Heat Exchanger of Pulse Tube Refrigerator, *International Journal of Heat and Mass Transfer*, 70, pp. 811–818

Tartibu, L.K., Kunene, T., 2019. Numerical Analysis of the Flow Pathlines in ThermoAcoustic Couples. *Procedia Manufacturing*, 35, pp. 246–251.

Versteeg, K., and Malalasekera, W., 2007, An Introduction to Computational Fluid Dynamics: The Finite Volume Method, 2nd edition, England: Pearson Education Limited, Chap. 3.

Wakeland, R.S., Keolian, R.M., 2004. Measurements of the Resistance of Parallel-Plate Heat Exchangers to Oscillating Flow at High Amplitudes. *J. Acoust. Soc. Am*, 115(5), pp. 2071.

Wang, G., Vanka, S. P., 1995. Convective Heat Transfer in Periodic Wavy Passages. *Int. J. Heat Mass Transfer*, 38 (17), pp. 3219-3230,

Weiyang, C., Mohd Saat, F.A.Z., 2016. Oscillatory Flow across Plates with different Shape of Edges. Journal of Mechanical Engineering and Technology, 8 (1), pp. 1053.

Wheatley, J., Hofler, T., Swift, G.W., Migliori, A., 1983. An Intrinsically Irreversible Thermoacoustic Heat Engine. J. Acous. Soc. Am., 74 (1), pp. 153–170.

Wong, Kaufui V., Hernandez, Aldo, 2012. A Review of Additive Manufacturing. International Scholarly Research Notices, vol. 2012, Article ID 208760, 10 pages.

Yu Z., Mao X., Jaworski A. J., 2014. Experimental Study of Heat Transfer in Oscillatory Gas Flow inside a Parallel-Plate Channel with an Imposed Axial Temperature Gradient. *International Journal of Heat and Mass Transfer*, 77, pp. 1023 -1032

Zhao T. and Cheng P., 1995. A Numerical Solution of Laminar Forced Convection in a Heated Pipe Subjected to a Reciprocating Flow. *Int. J. Heat Mass Transfer*., 38 (16), pp.3011-3022.

Zhao, T.S., Cheng, P., 1998. Heat Transfer In Oscillatory Flows. Annual Review of Heat Transfer, Begell House, Inc. Vol 9, Chapter 7.

Zoontjens L., Howard C.Q., Zander A.C., Cazzolato B.S., 2008. Numerical Comparison Of Thermoacoustic Couples with Modified Stack Plate Edges. International Journal of Heat and Mass Transfer, 51, pp. 4829–4840.

Zoontjens L., Howard C.Q., Zander A.C., Cazzolato B.S., 2009. Numerical Study of Flow and Energy Fields in Thermoacoustic Couples of Non-Zero Thickness. International Journal of Thermal Sciences, 48, pp. 733–746.

NOMENCLATURES

CHX1	cold heat exchanger 1
CHX2	cold heat exchanger 2
C	mesh count
c	speed of sound, m/s
c_p	specific heat capacity, J/kgK
d	heat exchanger channel height, m
D	domain inlet and outlet height
DR	drive ratio
E	internal energy, J
f	frequency, Hz
h	plate thickness, m
h_c	heat transfer coefficient, W/m^2.K
HEX	Heat exchanger
HHX	hot heat exchanger
k'	angular wavenumber, rad/m
k_f	thermal conductivity, W/mK
l	heat exchanger length, m
L	length of the computational domain, m
Nu	Nusselt number
p_1	pressure amplitude, Pa
p	pressure, Pa
Pr	Prandtl number
Pr_t	turbulence Prandtl number
q	heat flux, W/m^2
R_c	specific gas constant, J/kgK
Re	Reynolds number
t	time, s

T	fluid temperature, K, $°C$
T_p	Period of oscillation, s
u	velocity amplitude, m/s
u_{c2}	centreline velocity amplitude in CHX2
U	normalised velocity amplitude, m/s
v	velocity (y-component), m/s
x, y	spatial and transverse distance, m
y_o	half channel distance, m

Greek symbols

in	inlet of domain
inlet	inlet of heat exchanger
out	outlet of domain
outlet	outlet of heat exchanger
Δ	difference
δ	normalised vertical channel distance
δ_{ij}	Kronecker delta
δ_k	thermal penetration depth, m
δ_v	viscous penetration depth, m
ω	angular frequency, rad/s
ω_v	vorticity, l/s
ρ	density, kg/m^3
μ	viscosity, kg/m.s
μ_t	turbulent eddy viscosity, kg/m.s
ϕ	Phase angle, °
λ	wavelength, m
κ	turbulent kinetic energy, m^2/s^2
ξ	displacement amplitude, mm
σ	heat exchanger porosity
θ	normalised temperature

Subscripts

$crit$ critical
c cold
$c1$ cold heat exchanger 1 cold
$c2$ heat exchanger 2 effective
eff fluid condition Source term
f hot heat exchanger heat
G
h exchanger
hx arbitrary point mean value
ij maximum condition
m
max

mid	mid-point or centre
N	Source term
o	reference value or condition
Ref	reference value
1	amplitude, acoustic or oscillating variable
s	edge shape condition
t	turbulence
w	wall
sim	Simulation
sq	square-edge shape
cn	cone-edge shape
og	ogive-edge shape
rd	round-edge shape

List of figures

Fig. 3 (a) velocity amplitude against phase angle at DR = 0.3% (x/L = 4.80) (b) theoretical and predicted velocity amplitude vs. phase angle at DR = 0.3% (x/L = 4.80) (c) Measured and predicted Pressure amplitudes vs. phase angle for square-edge shape at DR = 0.3% (x/L = 4.79) (d) measured and predicted gas temperatures (T1, T2, T3 and T4) at $0.3 \leq DR \leq 1.5\%$.

Fig. 4 Velocity profiles vs. δ (y/d) at $0.3 \leq DR \leq 2.0\%$ (x/L = 4.79). In the legend, flow phases 1, 4 and 7 are represented for square-edge (sq) as sq_ ϕ1, sq_ϕ 4, and sq_ϕ 7, cone-edge (cn) as cn_ ϕ1, cn_ ϕ4, and cn_ ϕ7, ogive-edge (og) as og_ ϕ1, og_ ϕ4, and og_ ϕ7, and round-edge (rd) as rd_ ϕ1, rd_ ϕ4, and rd_ ϕ7.

Fig. 5 Centreline velocity profile at the middle of CHX2 (x/L = 4.80) for square (sq), cone (cn), ogive (og), and round (rd) edge shapes for ϕ4 (a) DR = 0.65% (b) DR = 1.0%.

Fig. 6 Velocity amplitudes vs. DR for square (sq), cone (cn), ogive (og) and round (rd) edge shapes (x/L = 4.79).

Fig. 7 Vorticity (1/s) contours for square, cone, ogive, and round edge shapes, respectively, at ϕ7 (a) DR = 0.3% (b) DR = 1.0%.

Fig. 8 Cross-sectional temperature profiles at $0.3 \leqslant DR \leqslant 2.0\%$ (x/L = 4.79). In the legend, the flow at phases 1, 4 and 7 are presented for square-edge (sq) as sq_ϕ1, sq_ϕ4 and sq_ϕ7, for cone-edge (cn) as cn_ϕ1, cn_ϕ4 and cn_ϕ7, for ogive-edge (og) as og_ϕ1, og_ϕ4 and og_ϕ7, and round-edge (rd) as rd_ϕ1, rd_ϕ 4 and rd_ϕ7.

Fig.9 Temperature profiles of CHX1, CHX2 and HHX for square (sq), cone (cn), ogive (og) and round (rd) edge shapes (a) inlet (b) centreline and (c) outlet. Locations a, b, and c (i.e. x/L = 4.79, x/L = 4.80, and x/L = 4.81). Similar locations are used for all heat exchangers.

Fig. 10 Space-cycle averaged heat flux vs. *DR* for CHX1, HHX and CHX2.

Fig. 11 Measured and predicted *Nu* vs. *DR*.

Fig. 12 Δp_1 vs. t/T_p for all edge shapes – square (sq), cone (cn), ogive (og), and round (rd) at *DR* = 0.3%, 1.0% and 2.0% (a) CHX1 (b) HHX (c) CHX2.

Fig. 13 Measured and predicted Δp_1 vs. t/T_p for square edge shape (sq) at p_m = 1 bar, *DR* = 1.4% across (a) HHX (b) CHX2.

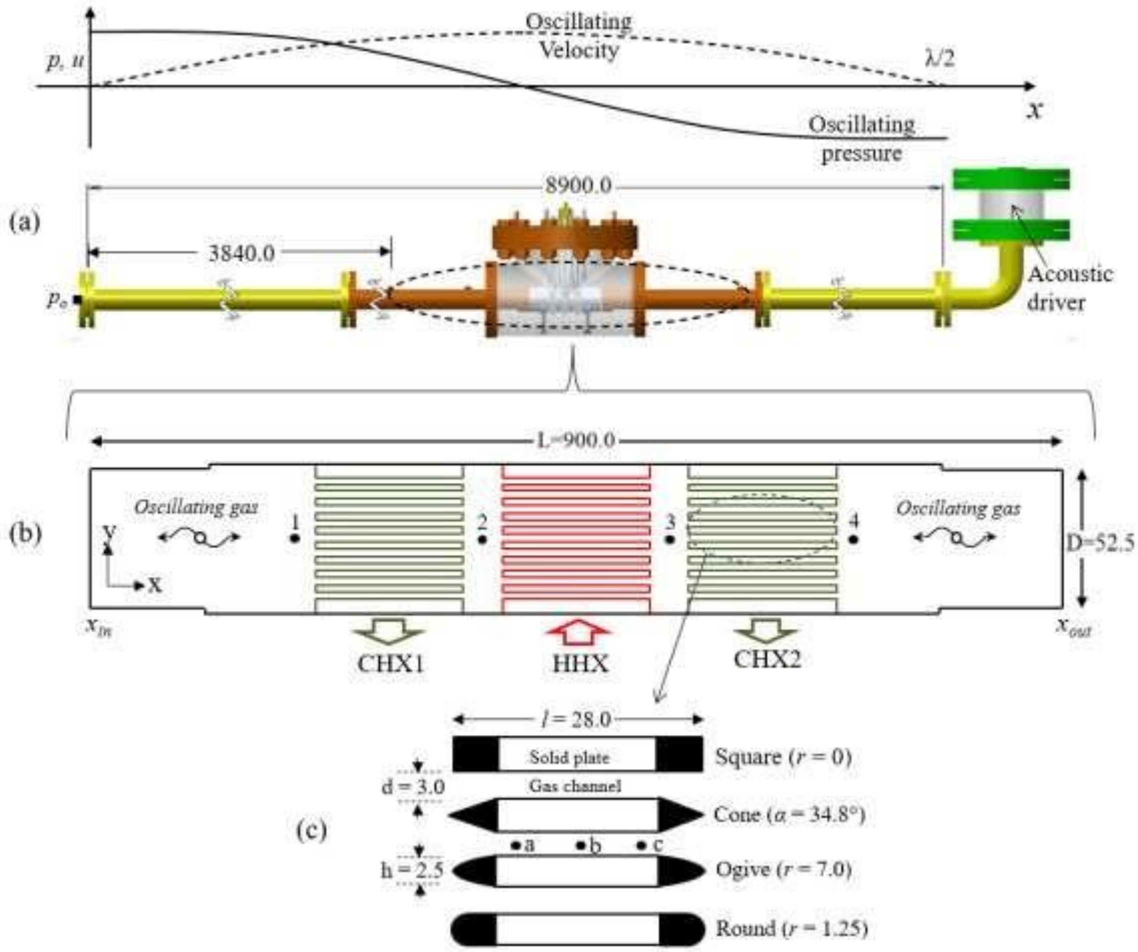

Fig. 1: (a) Schematic of experimental setup (b) Computational domain (c) Edge shapes – square, cone, ogive, and round shapes. Locations 1 (x/L = 4.72), 2 (x/L = 4.75), 3 (x/L = 4.79), 4 (x/L = 4.82), a (x/L = 4.79), b (x/L = 4.80) and c (x/L = 4.81) are used for data sampling. Oscillating variables are identified with numbers from their location (e.g., location 1 has temperature T1). Location 'a' is at 5 mm into the gas channel, measured from the stagnation point on edge shapes. All dimensions are in mm.

Fig. 2: Velocity and

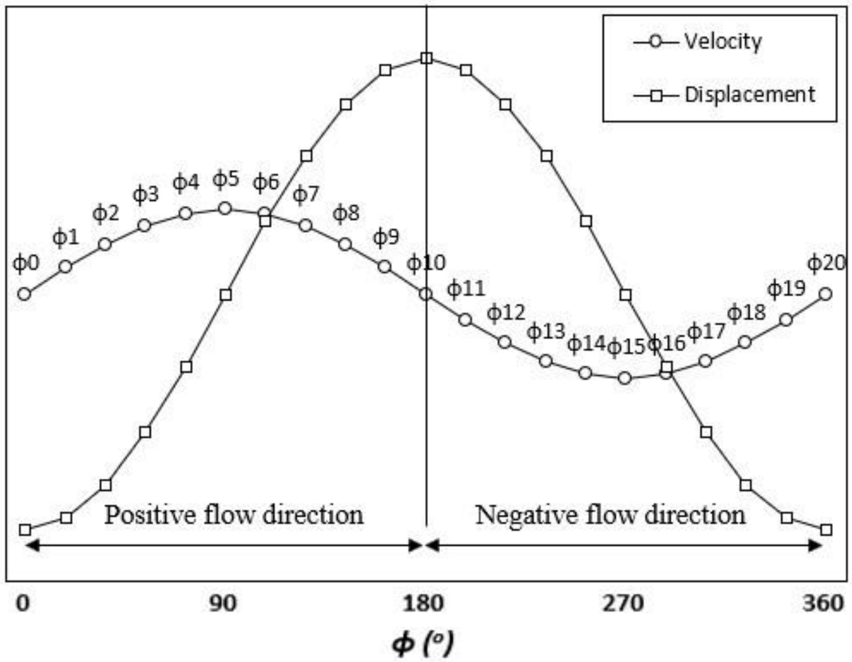

displacement amplitudes vs. phase angle (ϕ).

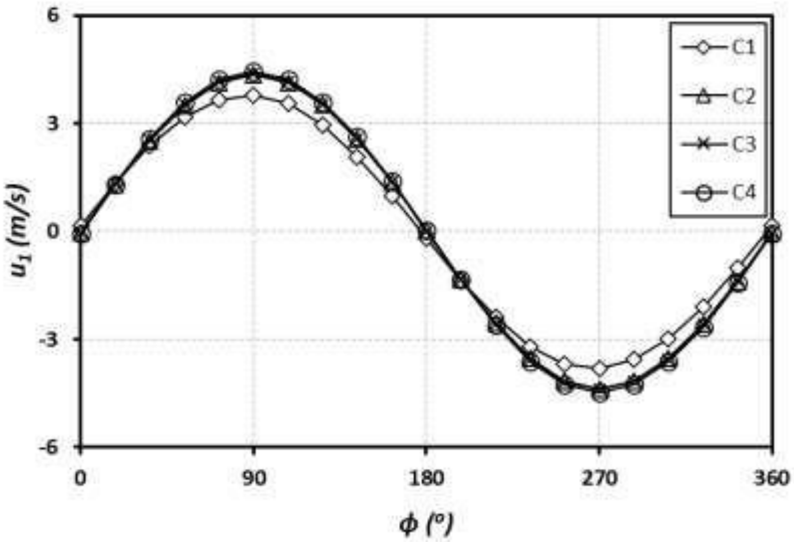

C1
C2
C3
C4
u1 (m/s)
ϕ (º)
6
3
0
-3
-6
0
90
180
270
360

(a)

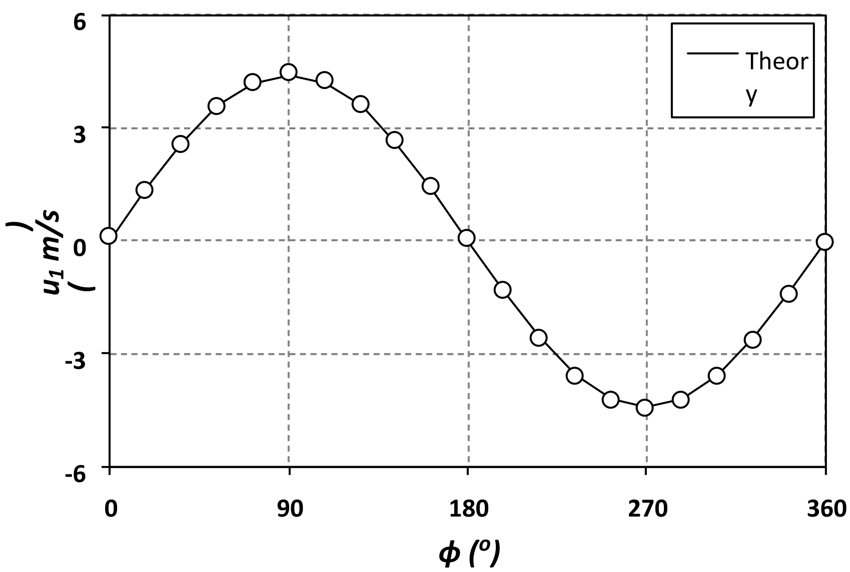

Theory
u1 (m/s)
ϕ (º)
6
3
0
-3
-6
0
90
180
270
360

(b)

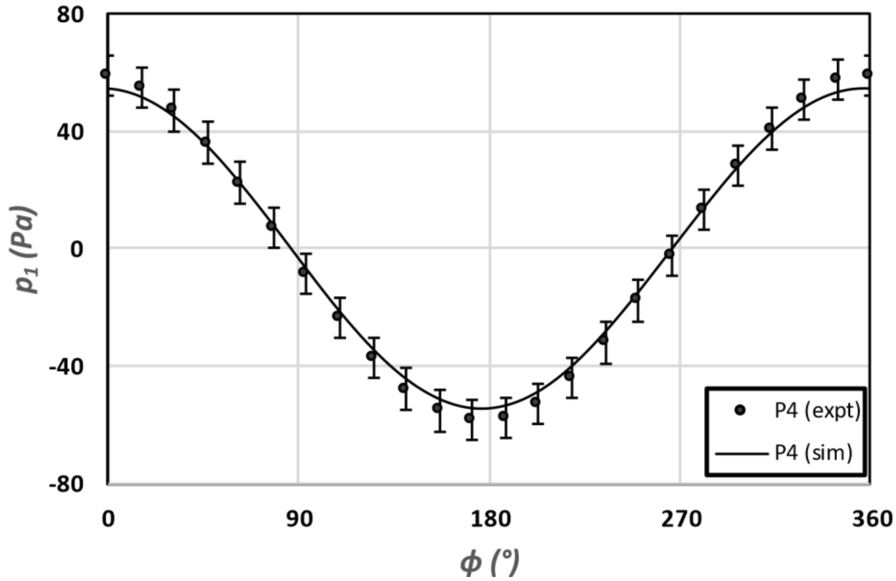

(c)

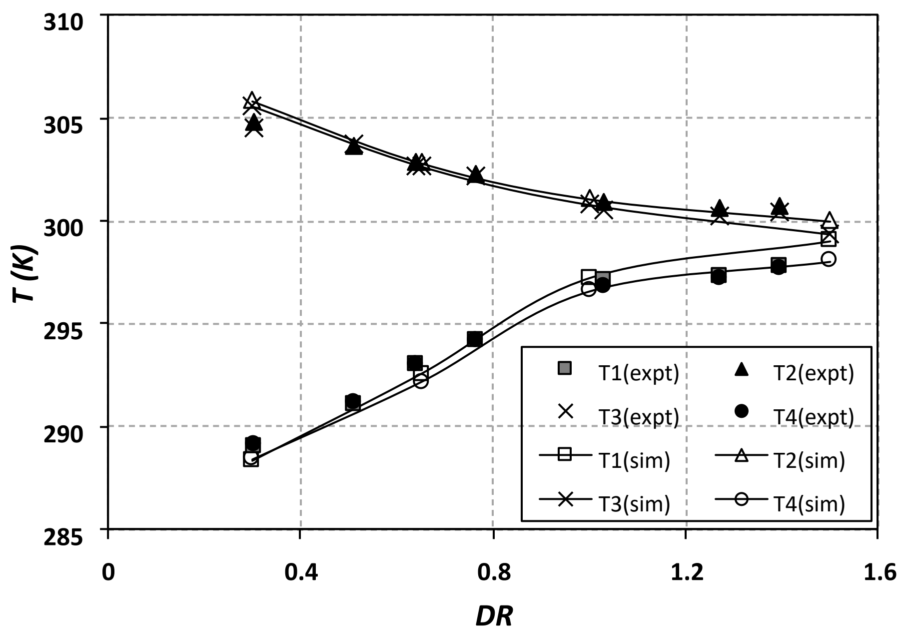

(d)

Fig. 3: (a) velocity amplitude against phase angle at *DR* = 0.3% (*x/L* = 4.80) (b) theoretical and predicted velocity amplitude vs. phase angle at *DR* = 0.3% (*x/L* = 4.80) (c) Measured and predicted Pressure amplitudes vs. phase angle for square-edge shape at *DR* = 0.3% (*x/L* = 4.79) (d) measured and predicted gas temperatures (T1, T2, T3 and T4) at $0.3 \leq DR \leq 1.5\%$.

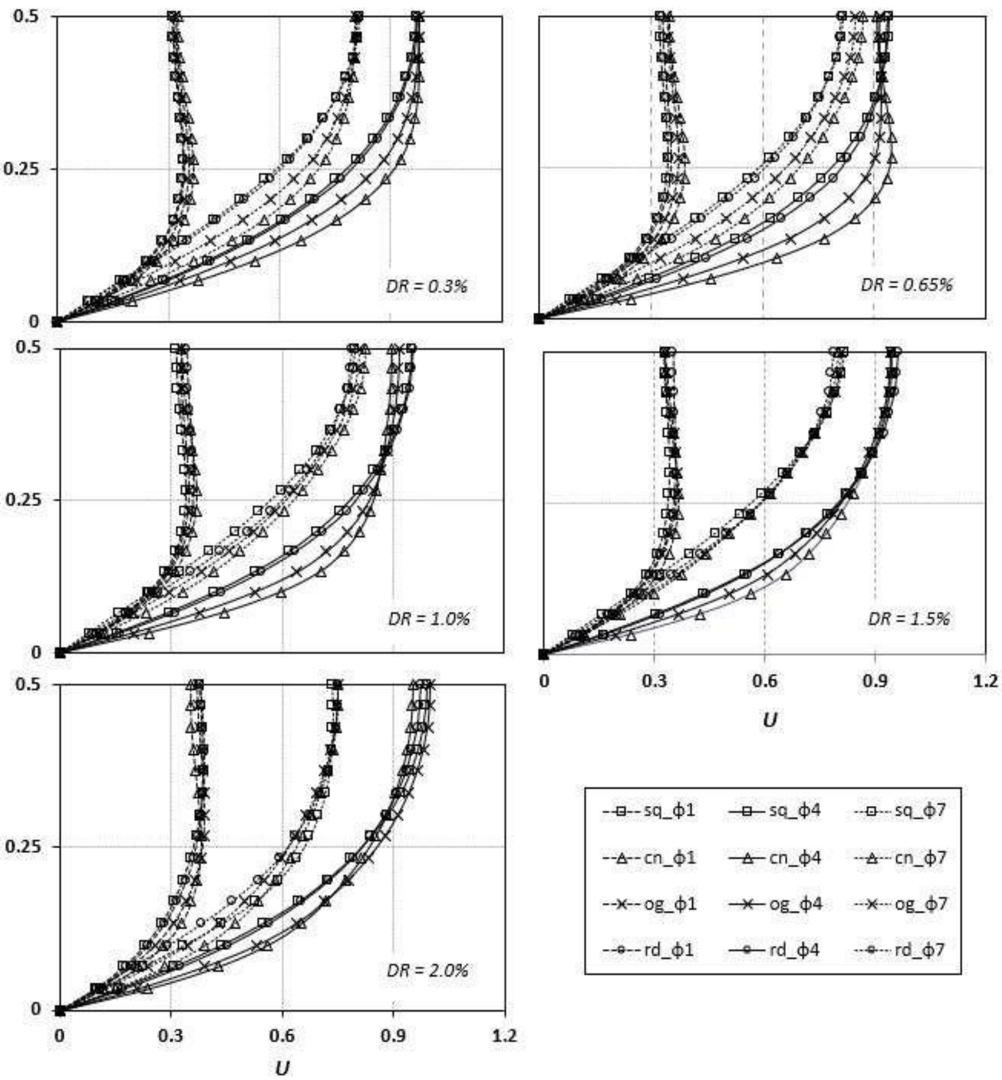

Fig. 4: Velocity profiles vs. δ (*y/d*) at $0.3 \leq DR \leq 2.0\%$ (x/L = 4.79).

In the legend, flow phases 1, 4 and 7 are represented for square-edge (sq) as sq_ ϕ1, sq_ ϕ4, and sq_ ϕ7, cone-edge (cn) as cn_ ϕ1, cn_ ϕ4, and cn_ ϕ7, ogive-edge (og) as og_ ϕ1, og_ ϕ4, and og_ ϕ7, and round-edge (rd) as rd_ ϕ1, rd_ ϕ4, and rd_ ϕ7.

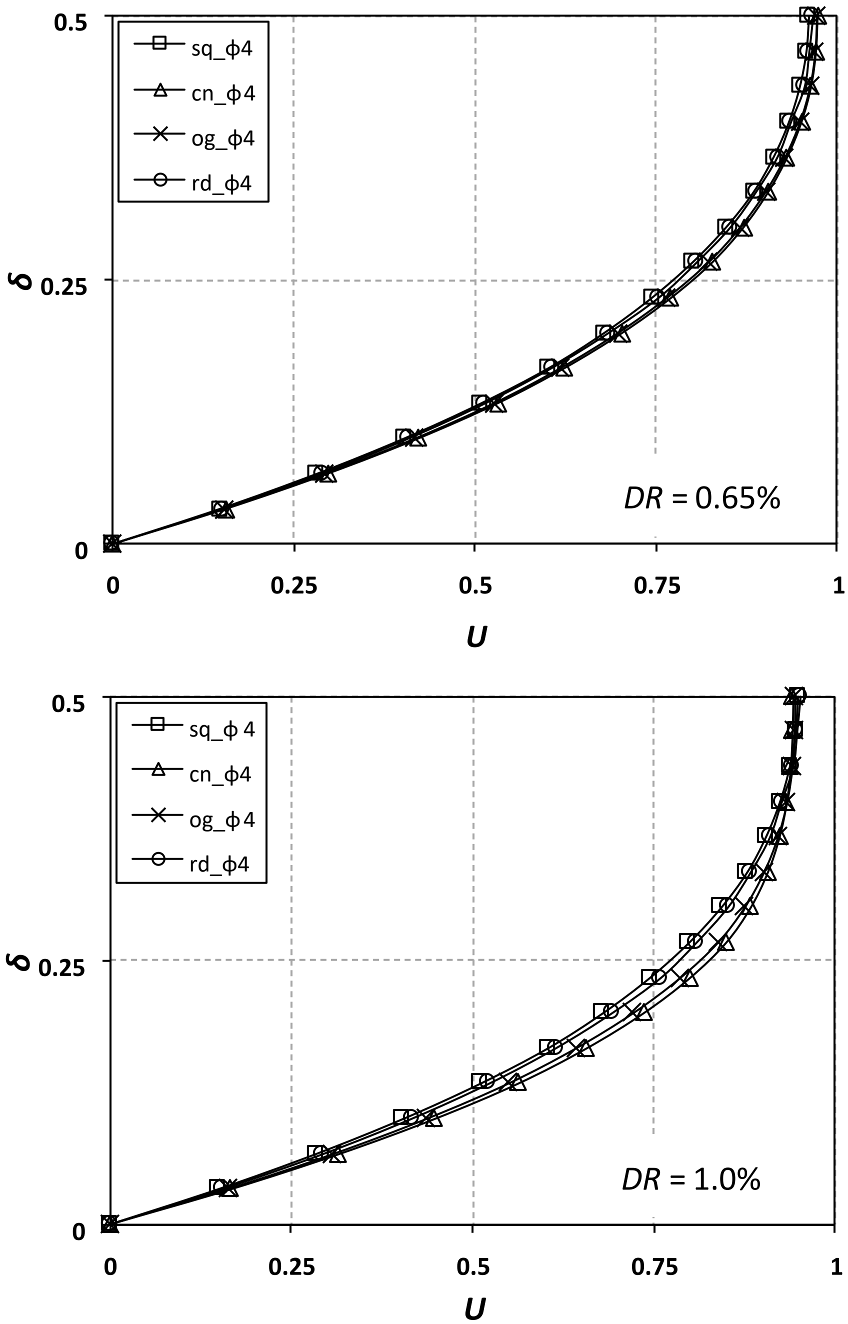

(a)

(b)

Fig. 5: Centreline velocity profile at the middle of CHX2 (x/L = 4.80) for square (sq), cone (cn), ogive (og), and round (rd) edge shapes for ϕ4 (a) DR = 0.65% (b) DR = 1.0%.

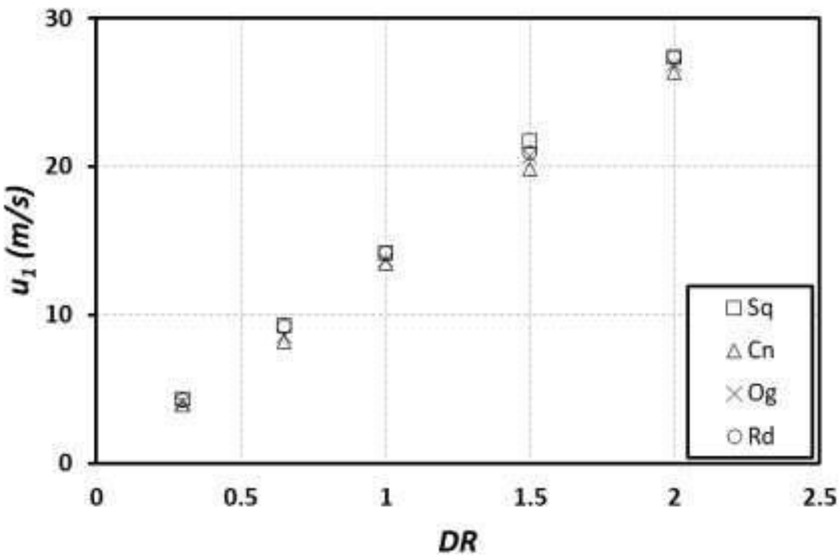

Fig. 6: Velocity amplitudes vs. *DR* for square (sq), cone (cn), ogive (og) and round (rd) edge shapes (x/L = 4.79).

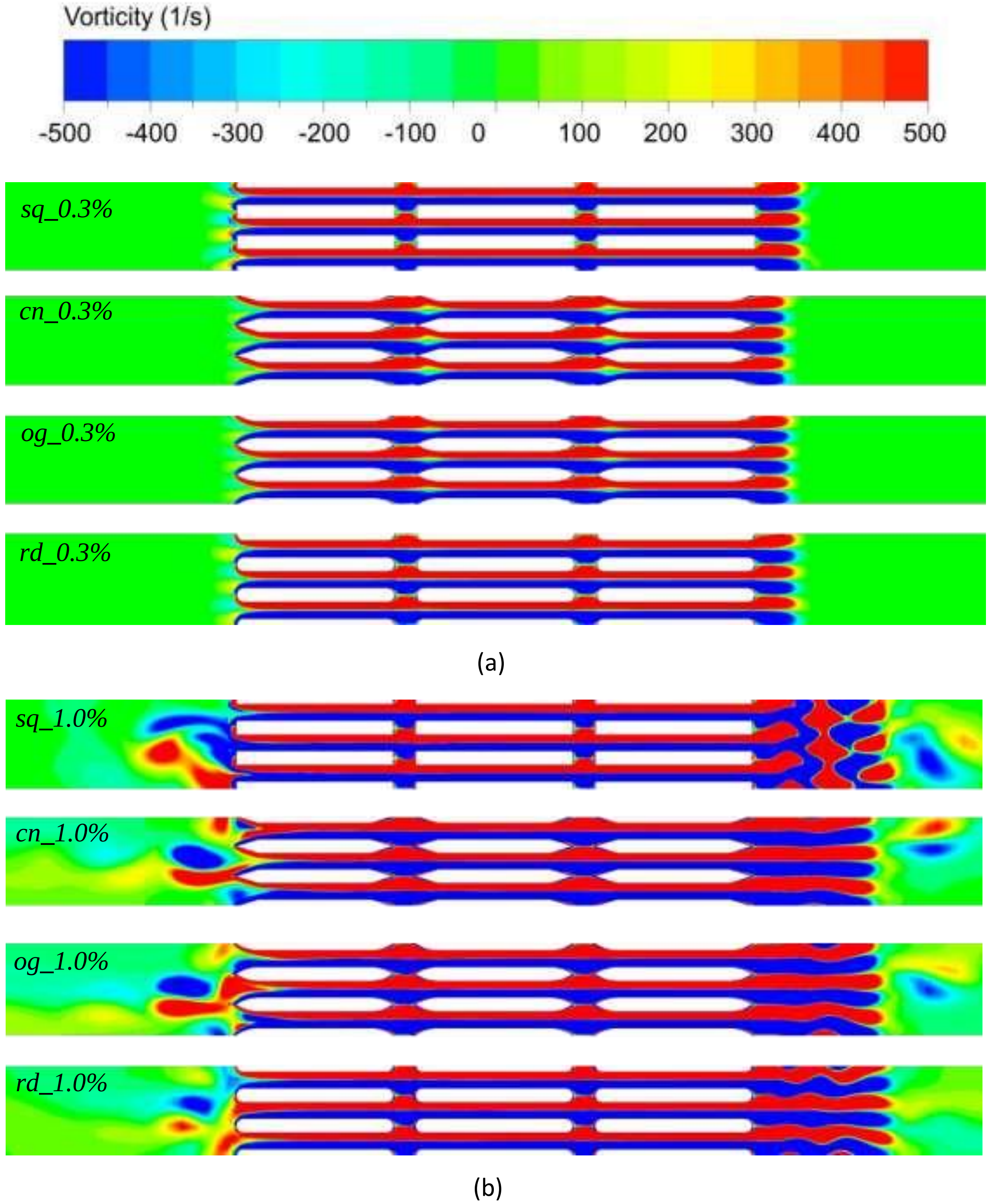

Fig. 7: Vorticity (1/s) contours for square, cone, ogive, and round edge shapes, respectively, at $\phi 7$ (a) DR = 0.3% (b) DR = 1.0%.

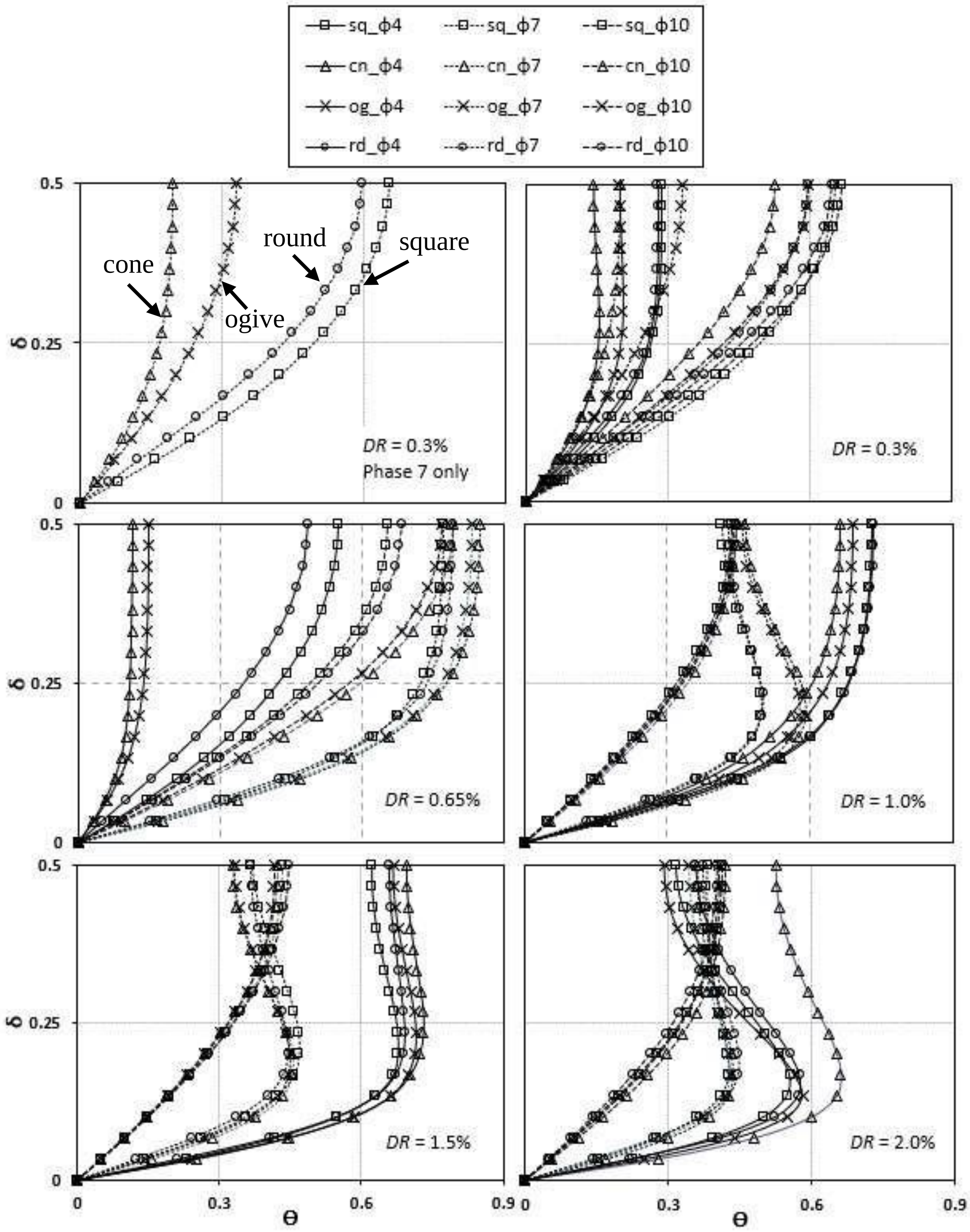

Fig. 8: Cross-sectional temperature profiles at $0.3 \leqslant DR \leqslant 2.0\%$ (x/L = 4.79). In the legend, the flow at phases 1, 4 and 7 are presented for square-edge (sq) as sq_ϕ1, sq_ϕ4 and sq_ϕ7, for cone-edge (cn) as cn_ϕ1, cn_ϕ4 and cn_ϕ7, for ogive-edge (og) as og_ϕ1, og_ϕ4 and og_ϕ7, and round-edge (rd) as rd_ϕ1, rd_ϕ4 and rd_ϕ7.

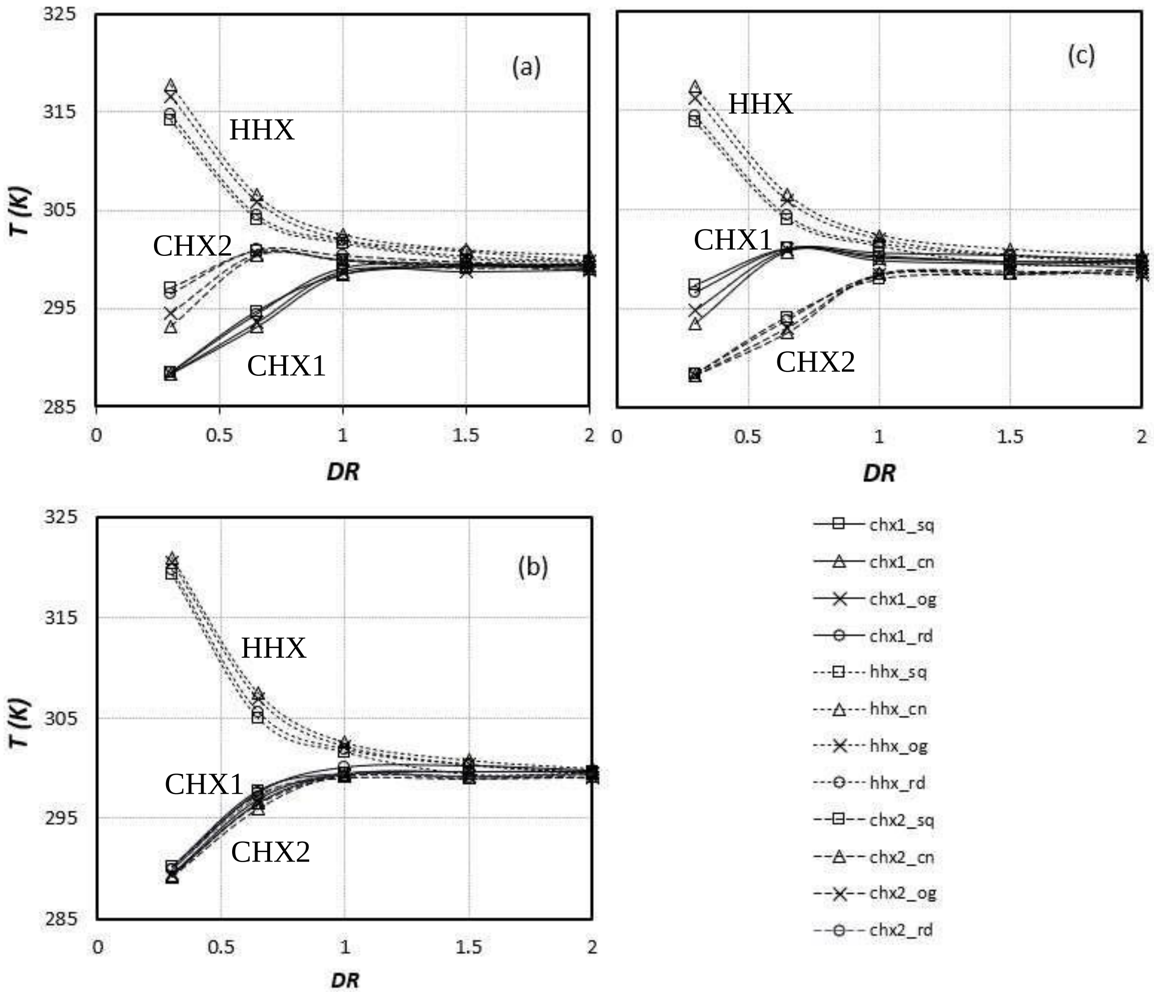

Fig. 9: Temperature profiles of CHX1, CHX2 and HHX for square (sq), cone (cn), ogive (og) and round (rd) edge shapes (a) inlet (b) centreline and (c) outlet. Locations a, b, and c (i.e. x/L = 4.79, x/L = 4.80, and x/L = 4.81). Similar locations are used for all heat exchangers.

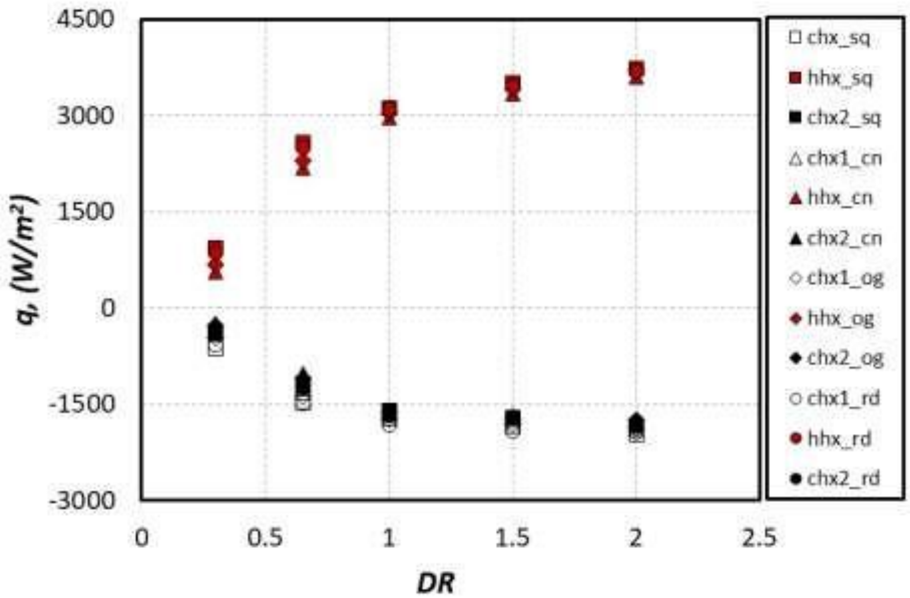

Fig. 10: Space-cycle averaged heat flux vs. *DR* for CHX1, HHX and CHX2.

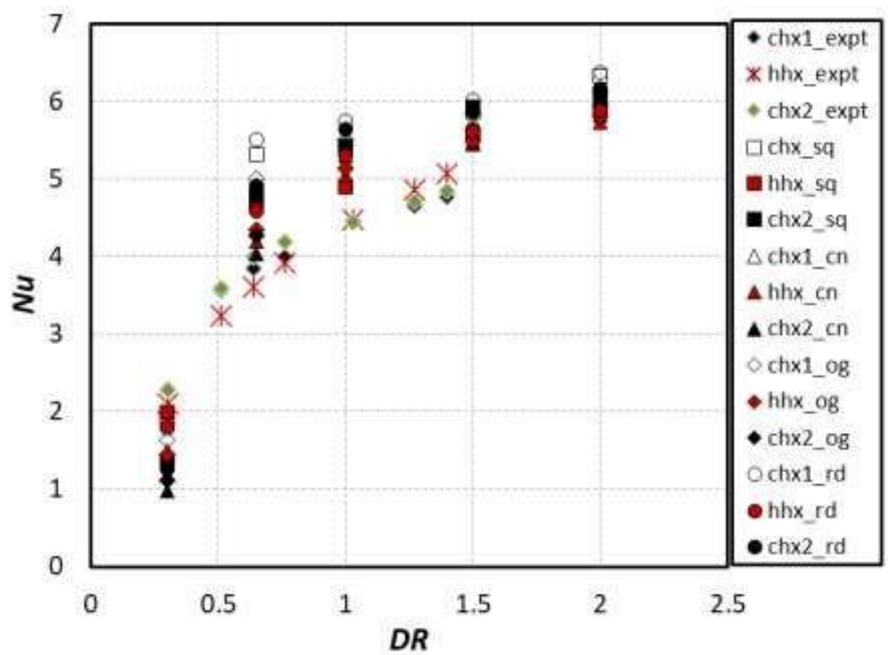

Fig. 11: Measured and predicted *Nu* vs. *DR.*

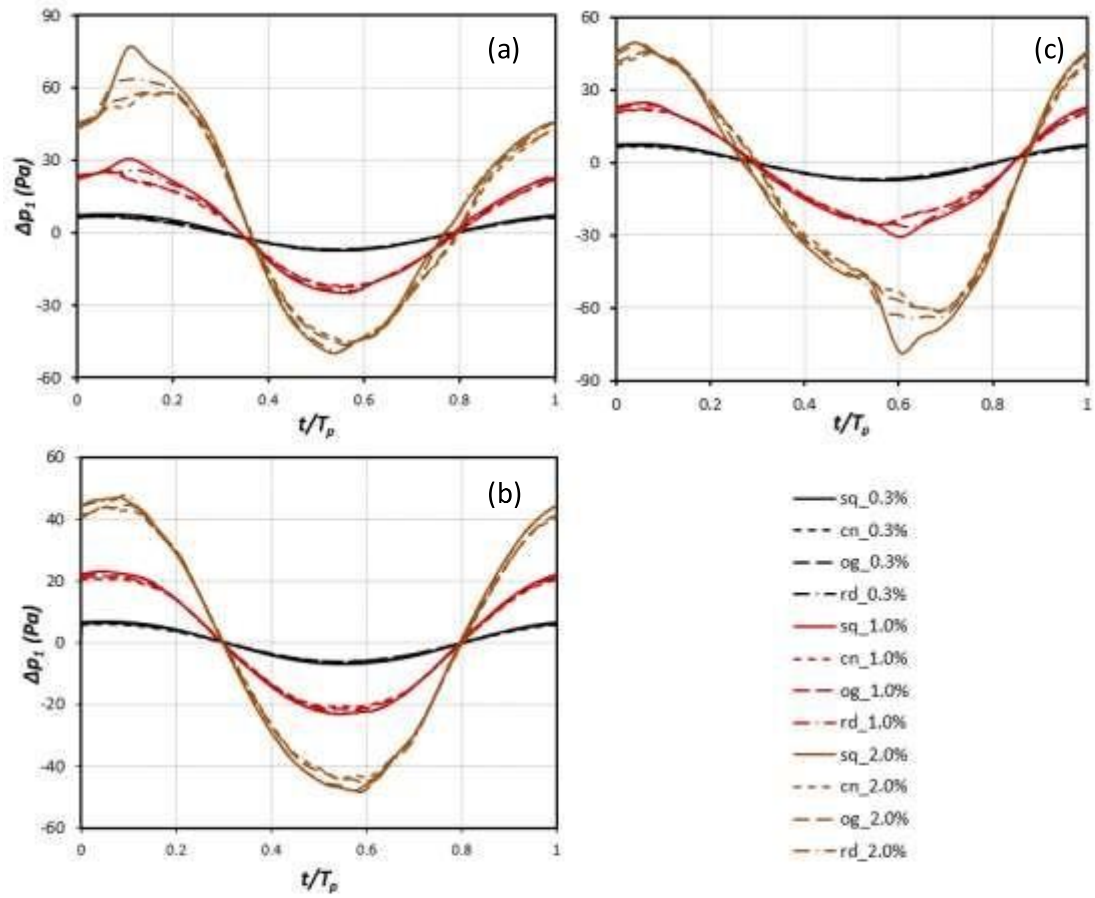

Fig. 12: Δp_1 vs. t/T_p for all edge shapes – square (sq), cone (cn), ogive (og), and round (rd) at DR = 0.3%, 1.0% and 2.0% (a) CHX1 (b) HHX (c) CHX2.

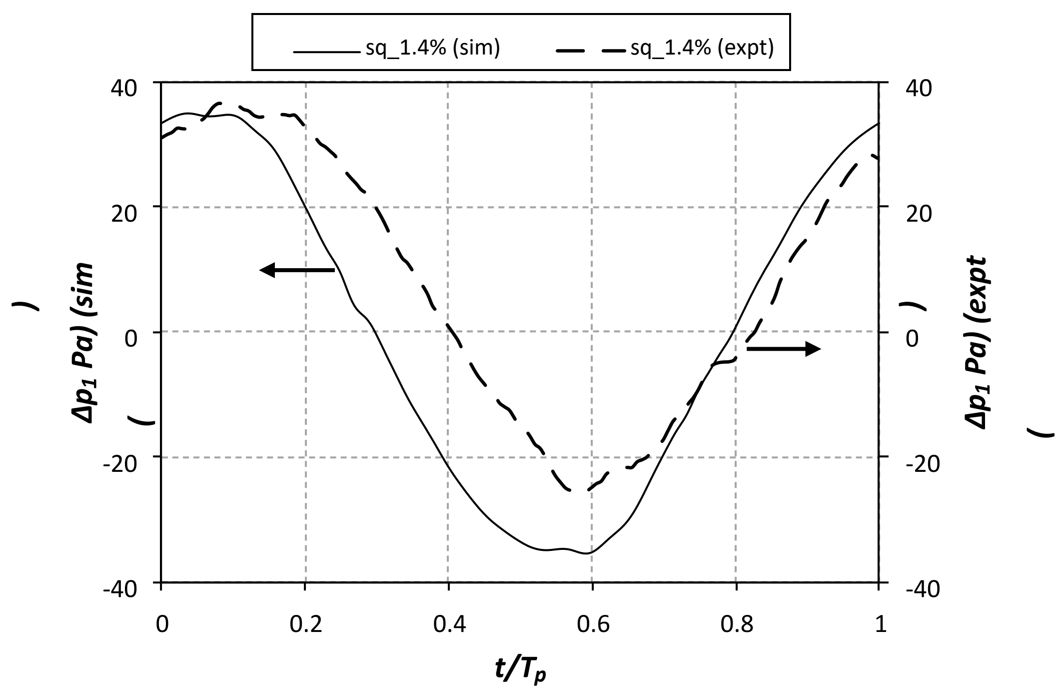

(a)

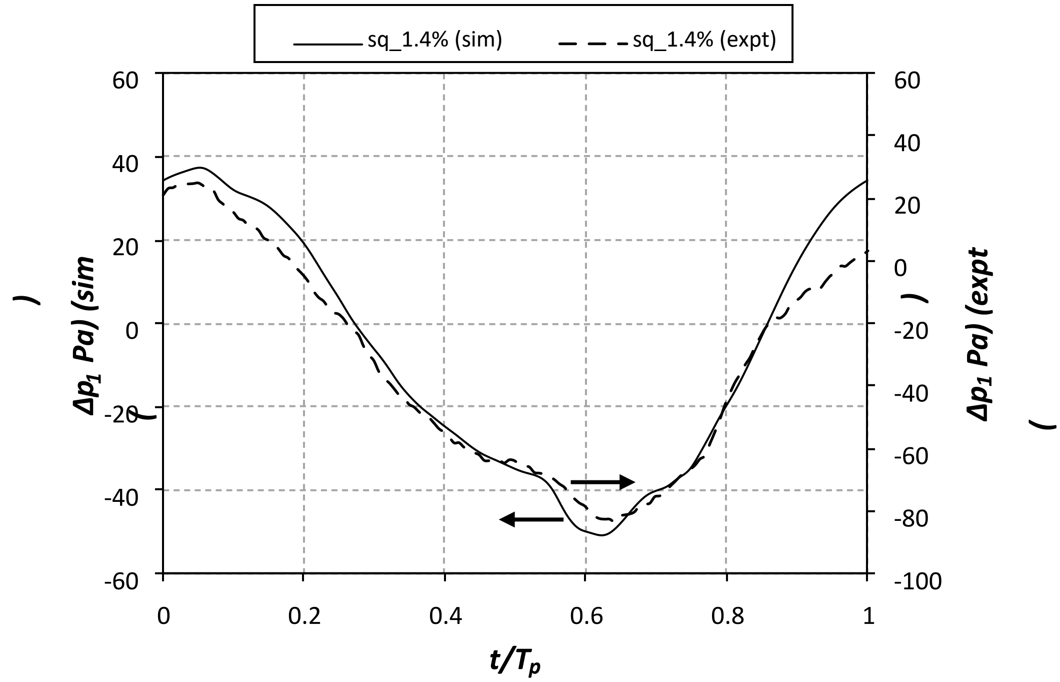

(b) Fig. 13: Measured and predicted Δp_1 vs. t/T_p for square edge shape (sq) at p_m = 1 bar,

DR = 1.4% across (a) HHX (b) CHX2.

List of Table

Table 1: Geometric and operating parameters for simulation

Parameters	**Values/descriptions**
Fluid	Helium
Mean pressure (p_m), MPa	0.1
Frequency (f), Hz	57.0
Drive ratio, %	$3 \leq DR \leq 2.0$
CHX1 surface temperature (T_{c1}), ºC	15.0
HHX surface temperature (T_h), ºC	50.0
CHX2 surface temperature (T_{c2}), ºC	15.0
Inlet boundary location, mm	3493.5
Outlet boundary location, mm	4393.5 0.

Table 2: simulation results for all edge shapes at $T_{c1,c2}$ = 15ºC, T_h = 50ºC, p_m = 1 bar and Re_1 = 96 – 672

DR (%)	Square		Cone		Ogive		Round	
	$u_{1,sq}$ (m/s)	T (K)	$u_{1,cn}$ (m/s)	T (K)	$u_{1,og}$ (m/s)	T (K)	$u_{1,rd}$ (m/s)	T (K)
0.3	4.3	313.7	3.9	307.5	4.1	310.9	4.2	313.1
0.65	9.3	314.9	8.2	317.9	8.6	317.3	9.2	316.3
1.0	14.2	313.5	13.5	313.4	13.7	314.1	14.2	313.7
1.5	21.7	310.8	19.9	311.1	20.7	311.4	20.9	312.3
2.0	27.4	310.5	26.4	311.2	26.9	310.5	27.4	311.9